Brandon A. Sforzo[1]
Argonne National Laboratory,
Lemont, IL 60439
e-mail: bsforzo@anl.gov

Aniket Tekawade
Argonne National Laboratory,
Lemont, IL 60439
e-mail: atekawade@anl.gov

Alan L. Kastengren
Argonne National Laboratory,
Lemont, IL 60439
e-mail: akastengren@anl.gov

Kamel Fezzaa
Argonne National Laboratory,
Lemont, IL 60439
e-mail: fezzaa@anl.gov

Jan Ilavsky
Argonne National Laboratory,
Lemont, IL 60439
e-mail: ilavsky@anl.gov

Christopher F. Powell
Argonne National Laboratory,
Lemont, IL 6043

Yuanjiang Pei
Aramco Research Center – Detroit,
Novi, MI 48377
e-mail: yuanjiang.pei@aramcoamericas.com

Anqi Zhang
Aramco Research Center – Detroit,
Novi, MI 48377
e-mail: anqi.zhang@aramcoamericas.com

Robert Levy
Aramco Research Center – Detroit,
Novi, MI 48377
e-mail: robert.levy@aramcoamericas.com

X-Ray Characterization of Real Fuel Sprays for Gasoline Direct Injection

The effects of fuel blend properties on spray and injector performance has been investigated in a side-mount injector for Gasoline Direct Injection (GDI) using two certification fuel blends: Euro 5 and Euro 6. Several X-ray diagnostic techniques were conducted to characterize the injector and spray morphology. Detailed internal geometry of the GDI injector was resolved to 1.8 μm, through the use of hard X-ray tomography. The geometry characterization of this six-hole GDI, side mount injector, quantifies relevant hole and counterbore dimensions and reveals the intricate details within the flow passages, including surface roughness and micron-sized features. Internal valve motion was measured with a temporal resolution of 20 μs and a spatial resolution of 2.0 μs, for three injection pressures and several injector energizing strategies. The needle motion for both fuels exhibits similar lift profiles for common energizing commands. A combination of X-ray radiography and ultra-small-angle X-ray scattering (USAXS) was used to characterize the fuel mass distribution and the droplet sizing, respectively. Tomographic spray radiography revealed the near-nozzle distribution of fuel mass for each of the fuels and the asymmetry produced by the angled nozzles. Under evaporative conditions, the two fuels show minor differences in peak fuel mass distribution during steady injection, though both exhibit fluctuations in injection during the early, transient phase. USAXS measurements of the path-specific surface area of the spray indicated lower peak values for the more evaporative conditions in the near nozzle region. [DOI: 10.1115/1.4050979]

Keywords: *energy from biomass, fuel combustion, Renewable energy*

Introduction

Improvements to the combustion efficiency and emissions output of internal combustion engines are driven by the strengthened regulation worldwide. Advancements to these system-level performance metrics in internal combustion engines, and more specifically, light-duty gasoline engines, hinge on improved behavior of fuel injection and atomization for new fuels and combustion technologies. Realizing these improvements requires predictive spray and chemical models, validated for realistic operating conditions.

Although combustion chemistry models are available for predicting new gasoline fuel blends [1–3], the tools depend on accurate input conditions, enabled by boundary conditions of fuel distribution, atomization, and evaporation behavior. Furthermore, central to the Department of Energy's program for Co-Optimizing fuels and engines, the Central Fuels Property Hypothesis [4] conjectures that the knock performance prediction behavior at the system-level traces to fuel properties. As a result, characterizing the injection behavior of real fuels is critical to enabling the combustion and system performance [5].

Additionally, as fuel blends trend toward higher ratios of oxygenates, and injection strategies push toward earlier conditions, flash boiling of the injected fuel is common. Historical efforts have focused spray studies on single component fuels [6], and this has been extended more recently to examine the plume behavior with modern GDI injection systems, where spray collapse has been characterized at these flashing conditions [7,8]. Encompassing models have therefore been developed to predict the spray based on injector and fuel information [9], though the spray behavior becomes more complicated with more complex distillate blends [10–13]. Therefore, understanding multi-component fuels at these conditions is valuable for improved understanding and predictive model validation.

This work will examine the internal characteristics, mechanical actuation, and spray morphology of a commercial GDI injector running real fuels, operating at several realistic conditions, through the use of X-ray diagnostics. X-ray studies permit quantitative measurements in optically opaque regions, such as inside the injector and

---

[1] Corresponding author.

Contributed by the Internal Combustion Engine Division of ASME for publication in the Journal of Energy Resources Technology. Manuscript received March 15, 2021; final manuscript received March 28, 2021; published online xx xx, xxxx. Assoc. Editor: Hameed Metghalchi.

within the optically dense near-nozzle region of the spray. When used as inputs to predictive simulations, the X-ray informed internal geometry has been shown to influence the spray morphology [14–16], and characterization of pintle motion has revealed transient internal flow phenomena [17]. Furthermore, quantitative fuel mass distributions, through X-ray radiography, provides important validation in the near-nozzle region [18], and the atomization information deduced from USAXS measurements has uniquely validated models for primary breakup [19,20]. All of these characterizations are of even further importance in understanding the behavior of injection with real fuels.

Methodology

Injection Equipment. The injector used in this study is a solenoid-actuated direct-acting GDI injector. The injector has six counterbored spray orifices, with the center of the spray plume at an angle to the injector axis. Fuel at pressures up to 30 MPa is provided to the injector by a pump-based high-pressure fuel system. While no common rail is used in this system, the volume of the line providing fuel to the injector is large compared to the injected volume. The injector is mounted in a temperature-controlled flange so the injector temperature is representative of the cylinder head temperature in operating engines. This flange is mounted to a spray chamber with X-ray transparent polyimide windows to permit spray and injector internal motion measurements, allowing control of the ambient pressure. This spray chamber also allows the injector to be rotated to acquire measurements from multiple lines of sight for spray tomography measurements. The chamber is purged with nitrogen at 4–10 L/min to remove stray fuel droplets and vapor. The target conditions for the measurements are shown in Table 1 and represent a range of spray conditions, from flash boiling (Condition 1) to purely liquid injection (Condition 3). Though the specific conditions evaluated for each diagnostic are presented subsequently, there has been specific focus on Condition 1 for spray quantification, which targets flash-boiling behavior.

Fuel Properties. For each of the examined conditions, two fuels were used, Euro 5 and Euro 6. These certification fuels of interest have subtle physical and chemical property variations. Table 2 lists select traits of the fuels which are known to influence spray morphology. Properties relating to the propensity for the fuel to flash-boil upon injection are specifically of interest for spray experiments at Condition 1. The influential properties at this condition would be the saturation pressure (P_{sat}) and the heat of vaporization (h_v), which differ by 5% and 2.7%, respectively. However, the property with the most significant contrast between the two fuels is the oxygenates content, differing by 49%. Although this particular property may not influence the spray and vaporization behavior, the oxygenate content can impact the distillation curve, which affects the flash-boiling behavior. The chemical properties are also presented to differentiate the fuels, specifically on reaction performance.

X-Ray Tomography. X-ray tomography was performed at the 7-BM beamline of the Advanced Photon Source (APS) to characterize the internal geometry of the injector using techniques previously detailed [21]. Specifically, the GDI injector was mounted on a rotation stage, and full-width X-ray projection images were captured at 4096 angles over a 180 deg span. Three full scans were performed and averaged together to increase the signal to noise ratio. Computed tomography was applied to these projections to reconstruct a density volume of the injector region of interest. The reconstructed dataset has a minimum resolved feature size of 2 μm [21] This 3D dataset was then binarized using CTSegNet [22,23], a segmentation package that uses convolutional neural networks, to extract the isosurface of the internal geometry of the injector. The resulting binary dataset was then used for metrology, and the isosurface was prepared for companion CFD simulations.

Table 1 Target conditions for radiography, pintle motion, and USAXS experiments

Condition	1	2	3
Injector temperature, K	363	363	363
Ambient temperature, K	323	323	323
Injection pressure, MPa	5	15	30
Ambient pressure, kPa	40	100	200
Injection command, ms	2	2	2

Table 2 Select physical and chemical properties of tested fuels at $P = 100$ kPa and $T = 363$ K

Property	Euro 5	Euro 6
Density μg/mm^3	684	678
P_{sat}, kPa	209.0	220
μ, N · s/m^2	2.46e−4	2.46e−4
σ, N/m	0.0153	0.0150
h_v, J/kg	4.64e5	4.77e5
H/C ratio	1.77	1.89
% vol Paraffinics	10.7	12.5
% vol Oxygenates	4.8	9.4

High-Speed X-Ray Imaging. High-speed X-ray imaging was performed at the 32-ID beamline [24] to capture dynamic motion of the internal pintle valve of the injector. The experimental setup is illustrated in Fig. 1, which uses a scintillator crystal, long-distance microscope, and visible-light camera to record the X-ray images. A Photron SA-Z high-speed camera recorded high-speed videos of the valve motion at 40 kHz for 40 injection events at each condition. These images were collected with a spatial resolution of 3.95 μm/pixel. The motion was imaged at each condition for two orthogonal perspectives, allowing for two views of the lift motion, and separate orthogonal captures of the lateral motion. An edge-tracking cross-correlation analysis was used to extract the axial and transverse motion of the pintle for the two perspectives. This methodology is further detailed in Ref. [25].

Spray Radiography. Quantitative measurements of the average liquid mass distribution of the spray issued from the injector were gathered using X-ray radiography, as illustrated in Fig. 2. The methodology is detailed in prior literature [26,27]. Here, the 8.0 ± 0.01 keV mean photon energy beam (4% ΔE/E) was focused (5 × 6 μm FWHM focus size) and passed through the spray. Incident beam (I_0) and transmitted beam (I) intensities were recorded with a temporal resolution of 3.68 μs, for sample periods synchronous with the injection command. These intensity traces were collected across a grid of Y–Z positions with respect to the injector and were ensemble averaged for 32 injection events at each spatial location. The injector could also be rotated about its axis for projections at different azimuthal (Θ) perspectives.

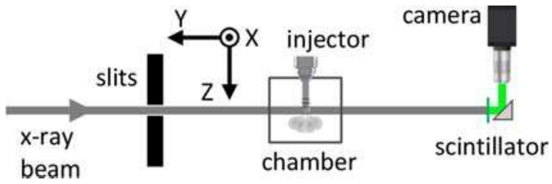

Fig. 1 Plan view of the imaging configuration used for dynamic pintle motion measurements and hard X-ray tomography for geometry characterization

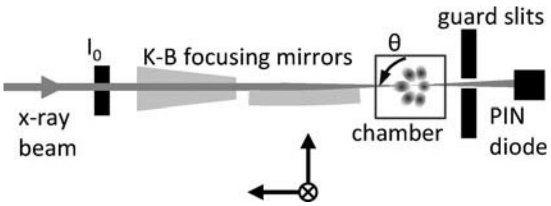

Fig. 2 Plan view of the radiography equipment

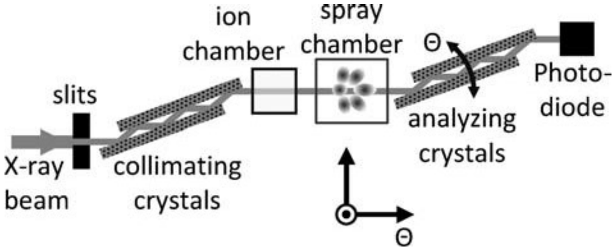

Fig. 3 Layout of the USAXS experiment

The projected mass of the spray (M) was computed from these traces using the Beer-Lambert law:

$$M(y, z, \theta, t) = -\frac{1}{\mu}\log\left[\frac{I(y, z, \theta, t)}{I_0(t)}\right] \tag{1}$$

where μ is the mass attenuation coefficient, which was empirically collected under the same instrument configuration as the experiment, $I_0(t)$ and $I(x, y, \theta, t)$ are the measured beam intensities of the incident beam and the transmitted beam, respectively. Computed tomography was applied to the projected density data to reconstruct the actual liquid density distribution on a cross-section of the spray.

Ultra-Small-Angle X-Ray Scattering. Quantitative measurements of the X-ray scattering of the GDI sprays were collected using the USAXS instrument at the 9-ID beamline of the APS [28], as shown in Fig. 3. The method for collection and processing of this scattering measurement for fuel sprays is detailed by Matusik et al. [29]. In short, a precisely collimated, 21 keV X-ray beam, profiled to 500 μm × 50 μm ($X \times Z$), was directed into the spray chamber during the steady-state portion of a lengthened (2 ms) spray event. For relatively dilute, homogeneous, and locally non-interacting particles, the scattered intensity follows Porod's Law [30], with the scattering intensity proportional to the total surface area of the scatterers in the beam. Full USAXS rocking curves were collected at least once for each axial location and condition, establishing the intensity profile for the probed scattering angles. Subsequent intensity measurements were made transversely across the spray at a fixed scattering angle, to understand the distribution of surface area across the spray cross section.

Results

Geometry. The internal flow geometry of this six-hole commercial GDI injector was characterized through hard X-ray tomography, with final resolved features of 2.0 μm, including internal surface roughness and imperfections. Two renderings of the injector tip isosurfaces are illustrated in Fig. 4, depicting the asymmetric hole orientation pattern of this side-mount injector design. The pintle is not depicted in the rendering on the right to allow a view of the shallow sac region. The coordinate system orientation defined for these studies is also depicted for each of the views, where the origin is located at the tip of the injector. The isosurface is also suitable and has been prepared for CFD boundary definition.

The reconstructed and segmented geometry were also used to make quantitative measurements of the internal features of the injector. The interior holes ranged in size from 145.2 μm to 165.7 μm, with a mean of 153 μm, while the counterbore diameters ranged from 293.3 μm to 298.6 μm with a mean of 296.3 μm. Due to the varying lengths and intersections with the interior and exterior surfaces, the hole lengths are not reported.

Pintle Motion. Pintle valve lift and wobble profiles based on high-speed X-ray imaging are plotted in Fig. 5. Each lift curve is the result of the average between the lift profiles of a given condition as viewed from two orthogonal perspectives (the X–Z and Y–Z planes), with the shaded region representing the standard deviation of the 80 tracked lift profiles. Lateral motion for each perspective was also tracked and plotted on the same axes for relative magnitude. From these profiles, it is evident that the injector pintle begins motion at 0.28 ms and repeatably lifts to a steady-state height of 60 μm by 0.5 ms after the commanded start of injection (SOI), then begins closing at 2.0 ms. All traces show overshoot at SOI, where the valve lift reaches a greater value than the steady-state value. The pintle wobble motions in either dimension follow the same periods as the lift, though the maximum deviation is approximately 5.5 μm, and the steady-state location is not concentric with the closed position. The wobble motion also exhibits a subtle oscillation, that lasts until approximately 1.0 ms. There is little variation in these traces between conditions. However, the injection pressure condition does influence the initial lift overshoot during the opening transient, with a maximum lift of 78 μm observed for Condition 3. The injection pressure also subtly influences the closing transient, with the higher pressure case closing about 80 μs earlier. It is assumed that the injection pressure has a greater influence on the mechanics of the pintle lift due to the fact that these values range from 5 to 30 MPa. Although the ambient pressure can play a role, the increase in ambient pressure from Condition 1 to Condition 3 represents 0.6% of the increase in injection pressure. Furthermore, the change in fuels has little influence on these values.

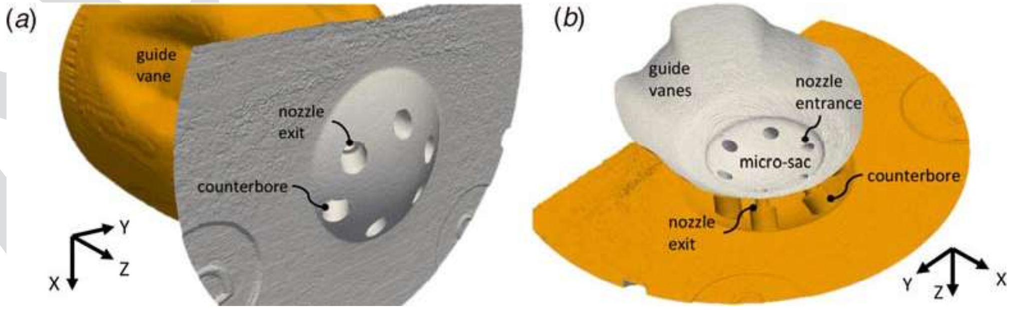

Fig. 4 Two renderings of the six-hole GDI injector geometry isosurface, produced from X-ray micro-CT

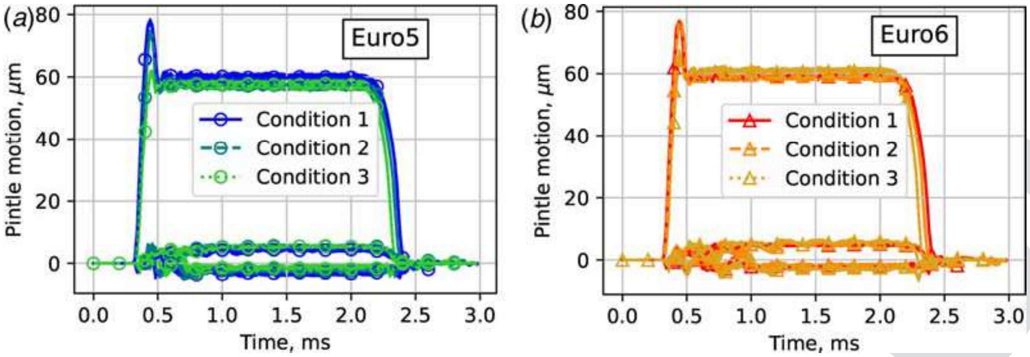

Fig. 5 Pintle motion traces in three orthogonal dimensions for the 6-hole GDI injector, for three target conditions, with each certification fuel

Spray Distribution. Fuel mass distributions were collected at Condition 1 for both fuels using X-ray radiography. Based on the vapor pressures of the fuels, listed in Table 2, this should result in flash-boiling of the fuel as it exits the injector. GDI sprays under these conditions have been previously characterized to exhibit rapid plume expansion, interaction, and collapse [31,32]. Although these previous studies focused on single component fuels, the present study using a multi-component fuel exhibits a similar expansion of the plumes from 1 to 5 mm, as seen in Fig. 6. The projected mass profiles for the two fuels are very similar, and both exhibit a broadening and blending of the plumes by the $Z = 5$ mm location. The asymmetric behavior of the individual plumes is also evident at $Z = 1$ mm in the tomographic reconstruction of the spray radiography for Euro 5. Sixty projection perspectives were used to generate the X–Y plane spray distribution plotted in Fig. 7. The skewed profile of this side-mount GDI injector is exhibited in this axial slice. It is also evident from this transverse slice that the plumes are blended and interacting since there are no voids in mass between the plumes. This is seen in the projected mass and the tomography data and is characteristic of the flash-boiling condition. This behavior can also lead to a recirculation zone in the central region and can contribute to plume collapse.

The radiography signal was sampled at 271.5 kHz capturing spray transient behavior. At each time-step, the projected mass profiles were spatially integrated according to Eq. (2), to calculate the transverse integrated mass (TIM), and are plotted in Fig. 8. This plot illustrates the arrival of mass to the 1 mm measurement plane by 0.3611 ms after SOI, and arrival to the 5 mm distance by 0.4326 ms after SOI, averaging 55.94 m/s. This arrival is consistent between the fuels, with an oscillatory behavior in mass/area exhibited by both after the initial transient. This is observed in the $Z = 1$ mm measurement, though it is enhanced at $Z = 5$ mm. These oscillations have been linked to the lateral pintle motion in prior works [33]; however, the duration of the fuel delivery oscillations persist beyond 1.0 ms, which is when pintle wobble motions become negligible. These histories also illustrate the relatively steady-state portion of the spray, existing between 1 and 2 ms after injection command. The mean TIM value for Euro 6 during this time range is approximately 6% lower than that for Euro 5, at both axial locations. Since the density of the two fuels only differs by 1%, this may indicate a spray morphology difference.

$$\mathrm{TIM}(z, t) = \int M_{\mathrm{fuel}}(y, z, t)\,\mathrm{d}y \tag{2}$$

Within a given case, the TIM is also related to the average velocity of the liquid through continuity. If the spray is at steady-state, the TIM is inversely proportional to the mass-averaged velocity, v_{ma} [34]. This can also be extended to compare separate cases, assuming the mass injection rate is consistent, and accounting for the liquid densities, as handled by:

$$\frac{v_{ma}}{v_{ref}} = \frac{\mathrm{TIM}_{ref}/\rho_{ref}}{\mathrm{TIM}/\rho} \tag{3}$$

The integrated mass ratio between the two fuels indicates a mean velocity of the Euro 6 spray 5–6% higher than the Euro 5 spray. This difference could be explained by the higher saturation pressure of Euro 6 fuel enhancing the flash boiling dynamics.

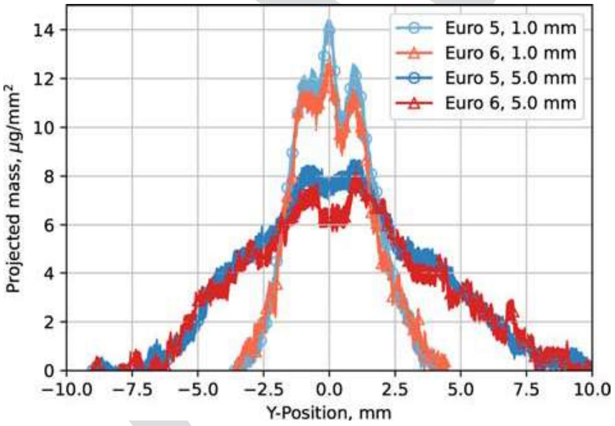

Fig. 6 Transverse scans of the projected mass for each fuel spray at 1 mm and 5 mm from the injector tip, averaged between 1 ms and 2 ms from the commanded start of injection, under Condition 1. Shaded bands indicate the standard deviation of the values during the steady state portion of injection.

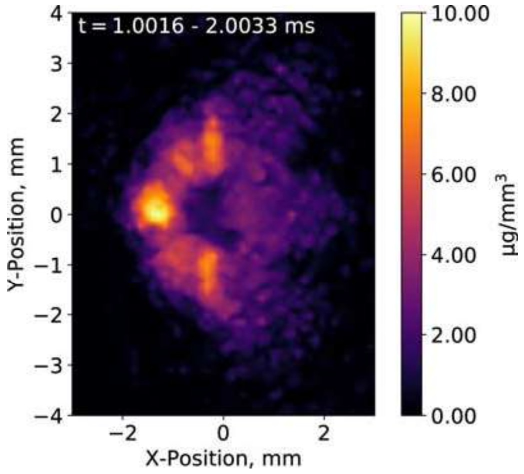

Fig. 7 Tomographic reconstruction of X-ray spray radiography, at $Z = 1$ mm, for Euro 5 fuel at Condition 1, time-averaged between 1.0 and 2.0 ms

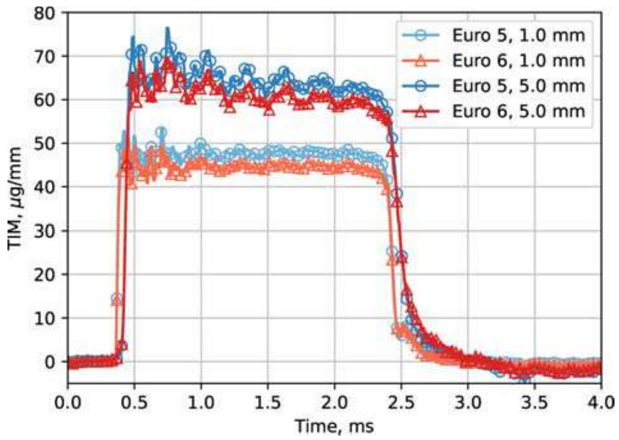

Fig. 8 Transverse integrated mass of X-ray spray radiography for each fuel at 1 mm and 5 mm from injector tip

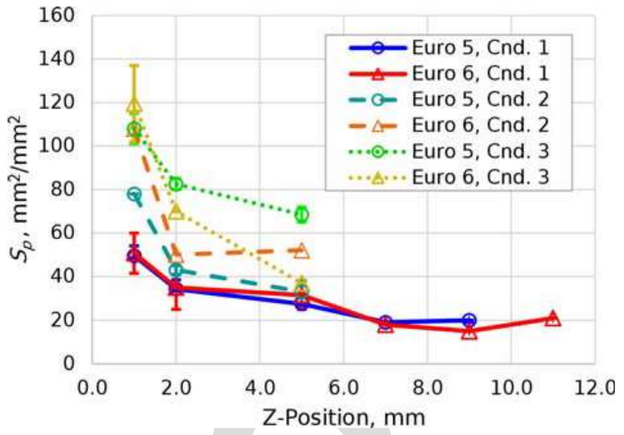

Fig. 10 Axial evolution of the specific surface area mean peak values (found near the transverse centerline) for each of the fuels at the three conditions

Furthermore, the TIM histories in Fig. 8 show an increase in the average steady-state TIM from the 1 mm to the 5 mm measurement location, revealing a mass-averaged velocity decrease in the spray by 12%. This deceleration of the spray is consistent with other studies linking the trend to the enhanced ambient gas entrainment designed for GDI injectors [35]. This contrasts the TIM evolution of diesel sprays with minimal entrainment in the near-field [26].

Spray Surface Area and Droplet Size. In addition to the mass distribution, the spray evolution is characterized by the level of atomization of the fuel. USAXS measurements were conducted and analyzed using similar procedures to previous works [29]. Transverse scans at fixed scattering vectors (q) were gathered to extract the path-specific surface area (S_p) of the spray, a measure of the interfacial area of the liquid–gas boundaries along the x-ray beam-path. A sample of the transverse scans are presented in Fig. 9 for Euro 5 at Condition 1, for the two orthogonal perspectives. In this example, the more symmetric spread across the Y-axis, and skewed distribution of spray along the X-axis is illustrated.

As the spray progresses downstream, the S_p peak value decreases and the signal spreads. The progress of this peak value near the center of the spray is shown in Fig. 10 for both fuels at the three conditions. These trends indicate a morphological difference in the spray between the three conditions, with higher near-nozzle S_p for the higher pressure cases, and a rapid drop in value as the spray progresses downstream. However, results at Condition 1 show a lower initial S_p which decreases gradually, in comparison to Condition 2 & 3 results over the same distance. Similar trends are observed for both fuels for these three cases.

The rapid decrease in S_p seen here is similar to the trends seen for a blend of 80% iso-octane and 20% ethanol (by volume) in a previous study [36] using a different fuel injector. Although absolute values for the S_p are more similar to a condition of pure iso-octane, it is important to examine the mass distribution to compare atomization characteristics between these experiments.

It should be noted that the S_p depends on both the number and size of droplets or upon the projected density of the spray and the average droplet size. Thus, a dilute spray with small droplets may have a similar S_p to a denser spray with larger droplets. Assuming that the measured spray consists of spherical droplets, the liquid volume measurements from radiography can be combined with the S_p values from the same probe volumes to yield the Sauter mean diameter (SMD, d_{32}), as was introduced in former works [37,38]. The relation,

$$d_{32} = 6\frac{V}{S_p} \tag{4}$$

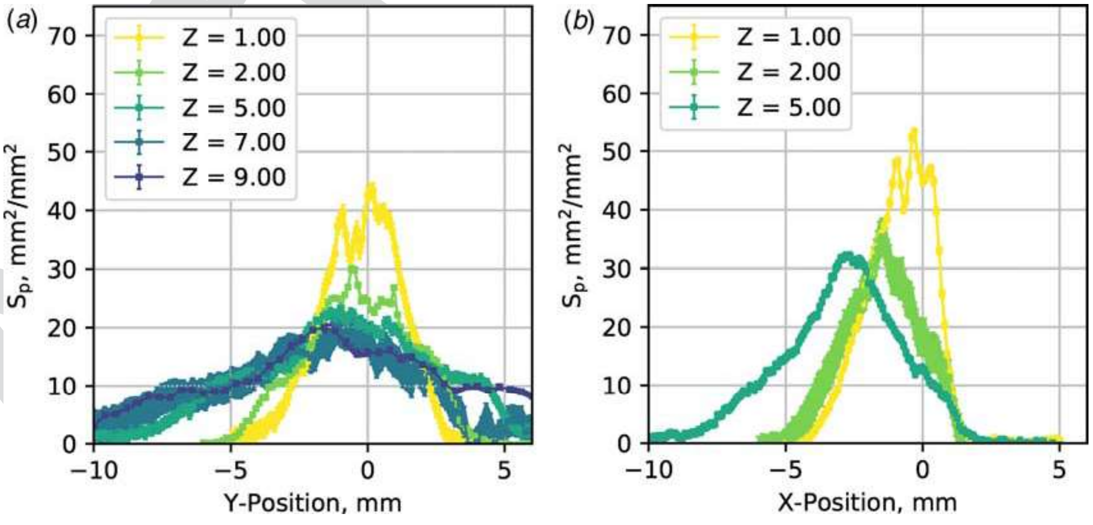

Fig. 9 Transverse profiles along the (*a*) *Y*-axis and (*b*) *X*-axis (right) of spray breakup for Euro 5 at Condition 1, for several axial distances

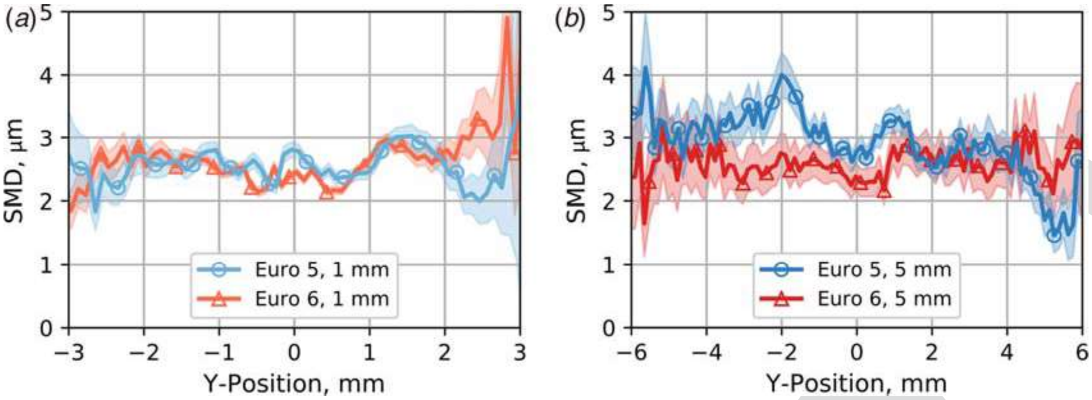

Fig. 11 Transverse profiles of SMD for both fuels at $Z = 1$ mm and $Z = 5$ mm, at Condition 1

was used, where S_p was collected through the USAXS measurements, and V obtained from radiography. The SMD values for both fuels, under Condition 1, are presented in Fig. 11, at $Z = 1$ mm and $Z = 5$ mm, where overlapping data existed for both USAXS and radiography.

In these profiles, the separation of the individual plume peaks are suppressed, which suggests that the droplet distribution is consistent in the transverse direction. At 1 mm from the injector tip, the SMD across the spray is roughly uniform at approximately 2.5 μm. This uniformity and average SMD across the spray persists to 5 mm with relatively consistent atomization behavior between the fuels. In a portion of the spray, there is indication of larger droplets for Euro 5, which, with evidence from the TIM profiles in Fig. 8, may indicate a subtle enhanced atomization for the Euro 6 fuel for this flashing condition, which can be caused by the preferential evaporation of distillate components. Furthermore, the evaporation of smaller droplets and concurrent evaporative cooling of larger droplets can selectively shift the SMD value when progressing downstream in the spray.

Overall, these results are similar in profile and magnitude to previous measurements of GDI sprays under flash-boiling conditions [36]. In these results, pure iso-octane at similar operating pressures and temperatures to the current study had a mean SMD of 8.0 μm, and a blend of iso-octane and ethanol resulted in SMD values of 0.8 μm. However, the current measurements show SMDs that are smaller than typically found using laser-based measurements of SMD in GDI sprays [39–42]. The current measurements differ from these measurements in several ways. First, the current results are measured close to the nozzle, in an optically dense region that is inaccessible to laser diagnostics, preventing a direct comparison between the two techniques. Second, the current results were measured under flash-boiling conditions. The rapid formation of internal voids under these conditions is expected to generate smaller droplets than purely shear-driven atomization and generate them quite close to the nozzle. The surface area-to-volume ratio of many small droplets will decrease the SMD, even in a distribution with larger droplets present. Finally, the smallest droplets will evaporate much more rapidly than the larger droplets. To first order, the droplet lifetime is expected to scale with the square of droplet diameter (d^2). As these droplets evaporate, they will cool the remaining fuel, making it evaporate more slowly. As such, the larger droplets from the near-nozzle region will persist at the more downstream locations typically probed with laser-based diagnostics. Since SMD is a mean of the distribution of sizes, it is an incomplete explanation of the droplet field, especially in these cases where there is a skewed distribution. As such, additional characterization of the near-to-far field atomization evolution is a continued research opportunity.

Conclusions

This work has presented the characterization of a six-hole GDI injector geometry and pintle motion under three realistic operating conditions. Furthermore, the spray liquid distribution from this injector was quantified under these conditions, specifically, varying injection pressure from 5 MPa to 30 MPa and ambient backpressure from 40 kPa to 200 kPa. For these conditions, two real certification fuels (Euro 5 & Euro 6) were used to explore the influence that subtle fuel property differences had on the injection mechanics and spray morphology.

Geometry characterization through X-ray CT revealed the internal features of the six-hole GDI injector, including the nozzle orientation and sizes. High-speed X-ray imaging allowed for the quantification of the internal pintle motion with both fuels, operating at all three test conditions. Results showed repeatable lift motion and steady-state position, with some lift overshoot for the higher injection pressure conditions. This overshoot points to elastic behavior of the injector structure, which can be explored and characterized further. Lateral pintle motion was also presented and exhibits some oscillatory behavior, and a steady-state lifted position that is not concentric with the closed position.

Spray mass distribution quantification through X-ray radiography illustrated the spray plume interaction for Condition 1 in transverse profiles and through tomographic reconstruction at 1 mm from the injector. The rapid expansion and merging of the plumes resembled similar flashing behavior observed in previous GDI studies [7,36], with single component fuels. In contrast, the fuel mass flux exhibited oscillatory behavior, seen in the transverse integration of the projected mass, despite constant pintle lift behavior during the same time period. Pintle wobble, which does exhibit some oscillatory motion, does not last the full duration of the dynamics seen in the spray. The pulsing may be an effect of multi-component fuel atomization behavior, possibly coupled with pressure wave dynamics within the injector, and merits additional investigation.

Repeatability between the fuels extended to the atomization behavior seen through x-ray scattering diagnostics. Specific surface area profiles tend to be unimodal for the Condition 1 results and decreased in peak value as the spray evolved downstream. More rapid decrease in peak S_p was noted for the higher pressure conditions. These surface area profiles were combined with the liquid volume information from radiography to calculate SMD for Condition 1 at two positions, revealing droplet sizes of 2.5 μm at 1 mm, and up to 4 μm at discrete locations by 5 mm. The largest separation in atomization behavior was seen at this 5 mm position in SMD values for the two fuels. These results also inspire additional investigation to connect the evolution of atomization from the near-to-far field.

This work serves as a preliminary presentation of real fuel spray behavior in the near-nozzle region. Furthermore, with the information gathered and provided to characterize the geometry and pintle motion, additional numerical studies are enabled by the inflow boundary conditions. The spray distribution and atomization information furnishes quantitative metrics for model development and validation of tools for multi-component fuel injection behavior.

Improved models for these real fuels will enable predictive capabilities and design for future fuels, injectors, and combustion systems.

Acknowledgment

Research presented in this paper was performed at the 7-BM, 9-ID, and 32-ID beamlines at the Advanced Photon Source at Argonne National Laboratory. Use of the APS is supported by the U.S. Department of Energy (DOE) under Contract No. DEAC0206CH11357. Argonne fuel spray research is sponsored by the DOE Vehicle Technologies Program under the direction of Gurpreet Singh and Michael Weismiller.

Conflict of Interest

There are no conflicts of interest.

References

[1] Sarathy, S., Thomson, M., Togbé, C., Dagaut, P., Halter, F., and Mounaim-Rousselle, C., 2009, "An Experimental and Kinetic Modeling Study of n-Butanol Combustion," Combust. Flame, **156**(4), pp. 852–864.

[2] Cai, L., and Pitsch, H., 2015, "Optimized Chemical Mechanism for Combustion of Gasoline Surrogate Fuels," Combust. Flame, **162**(5), pp. 1623–1637.

[3] Kohse-Höinghaus, K., Oßwald, P., Cool, T. A., Kasper, T., Hansen, N., Qi, F., Westbrook, C. K., and Westmoreland, P. R., 2010, "Biofuel Combustion Chemistry: From Ethanol to Biodiesel," Angew. Chem. Int. Ed., **49**(21), pp. 3572–3597.

[4] Szybist, J. P., and Splitter, D. A., 2018, "Understanding Chemistry-Specific Fuel Differences At a Constant Ron in a Boosted Si Engine," Fuel, **217**, pp. 370–381. Q5

[5] Pal, P., Kalvakala, K., Wu, Y., McNenly, M., Lapointe, S., Whitesides, R., Lu, T., Aggarwal, S. K., and Som, S., 2020, "Numerical Investigation of a Central Fuel Property Hypothesis Under Boosted Spark-ignition Conditions," ASME J. Energy Res. Technol., **143**(3), p. 12.

[6] Brown, R., and York, J. L., 1962, "Sprays Formed by Flashing Liquid Jets," AIChE J., **8**(2), pp. 149–153.

[7] Zhang, G., Xu, M., Li, T., Grover, R., Kuo, T., and He, Y., 2014, "A Study of Near-Field Spray Structure Under Superheated Conditions of a Gasoline Fuel Spray," ILASS Americas 26th Annual Conference on Liquid Atomization and Spray Systems, no. 68, ILASS Americas. Q6

[8] Blessinger, M., Manin, J., Skeen, S. A., Meijer, M., Parrish, S., and Pickett, L. M., 2015, "Quantitative Mixing Measurements and Stochastic Variability of a Vaporizing Gasoline Direct-injection Spray," Int. J. Engine Res., **16**(2), pp. 238–252.

[9] Lacey, J., Poursadegh, F., Brear, M., Gordon, R., Petersen, P., Lakey, C., Butcher, B., and Ryan, S., 2017, "Generalizing the Behavior of Flash-Boiling, Plume Interaction and Spray Collapse for Multi-hole, Direct Injection," Fuel, **200**, pp. 345–356.

[10] Sher, E., and Elata, C., 1977, "Spray Formation From Pressure Cans by Flashing," Ind. Eng. Chem. Process, **16**(2), pp. 237–242.

[11] Sharma, N., and Agarwal, A. K., 2020, "Particulate Morphology Characterization of Butanol–gasoline Blend Fueled Spark-Ignition Direct Injection Engine," ASME J. Energy Res. Technol., **142**(10). Q7

[12] Zeng, Q., Zeng, D., and Zheng, D., 2020, "Characteristics and Kinetic Analysis of Ignition for Different Gasoline Surrogate Fuel Models," ASME J. Energy Res. Technol., **142**(8).

[13] Roy, S., Zare, S., and Askari, O., 2019, "Understanding the Effect of Oxygenated Additives on Combustion Characteristics of Gasoline," ASME J. Energy Res. Technol., **141**(2).

[14] Yue, Z., Battistoni, M., and Som, S., 2020, "Spray Characterization for Engine Combustion Network Spray G Injector Using High-Fidelity Simulation With Detailed Injector Geometry," Int. J. Engine Res., **21**(1), pp. 226–238.

[15] Agarwal, A., and Trujillo, M. F., 2018, "A Closer Look At Linear Stability Theory in Modeling Spray Atomization," Int. J. Multiphase Flow, **109**, pp. 1–13.

[16] Saha, K., Som, S., Battistoni, M., Li, Y., Quan, S., and Kelly Senecal, P., 2016, "Modeling of Internal and Near-Nozzle Flow for a Gasoline Direct Injection Fuel Injector," ASME J. Energy Res. Technol., **138**(5).

[17] Baldwin, E., Grover, R., Parrish, S., Duke, D., Matusik, K., Powell, C., Kastengren, A., and Schmidt, D., 2016, "String Flash-Boiling in Gasoline Direct Injection Simulations With Transient Needle Motion," Int. J. Multiphase Flow, **87**, pp. 90–101.

[18] Nocivelli, L., Sforzo, B. A., Tekawade, A., Yan, J., Powell, C. F., Chang, W., Lee, C.-F., and Som, S., 2020, "Analysis of the Spray Numerical Injection Modeling for Gasoline Applications," SAE Technical Paper, SAE International.

[19] Pandal, A., Pastor, J. M., Payri, R., Kastengren, A., Duke, D., Matusik, K., Giraldo, J. S., Powell, C., and Schmidt, D., 2017, "Computational and Experimental Investigation of Interfacial Area in Near-Field Diesel Spray Simulation," SAE Int. J. Fuels Lubr., **10**(2), pp. 423–431.

[20] Battistoni, M., Magnotti, G. M., Genzale, C. L., Arienti, M., Matusik, K. E., Duke, D. J., Giraldo, J., Ilavsky, J., Kastengren, A. L., Powell, C. F., and Marti-Aldaravi, P., 2018, "Experimental and Computational Investigation of Subcritical Near-Nozzle Spray Structure and Primary Atomization in the Engine Combustion Network Spray D," SAE Int. J. Fuels Lubr., **11**(4), pp. 337–352.

[21] Matusik, K. E., Duke, D. J., Kastengren, A. L., Sovis, N., Swantek, A. B., and Powell, C. F., 2018, "High-Resolution X-ray Tomography of Engine Combustion Network Diesel Injectors," Int. J. Eng. Res., **19**(9), pp. 963–976.

[22] Tekawade, A., Sforzo, B. A., Matusik, K. E., Kastengren, A. L., and Powell, C. F., 2019, "High-fidelity Geometry Generation From CT Data Using Convolutional Neural Networks," *Developments in X-Ray Tomography XII*, B. Müller, and G. Wang, eds., Vol. 11113, International Society for Optics and Photonics, SPIE, p. 435–445. Q8

[23] Tekawade, A., 2020, [Online], "Ctsegnet: An End-to-End 3d Segmentation Package for Large X-Ray Tomographic Datasets," https://github.com/aniketkt/CTSegNet

[24] Shen, Q., Lee, W.-K., Fezzaa, K., Chu, Y. S., Carlo, F. D., Jemian, P., Ilavsky, J., Erdmann, M., and Long, G. G., 2007, "Dedicated Full-Field X-Ray Imaging Beamline At Advanced Photon Source," Nucl. Instrum. Methods Phys. Res. Sect. A, **582**(1), pp. 77–79.

[25] Kastengren, A. L., Tilocco, F. Z., Powell, C. F., Manin, J., Pickett, L. M., Payri, R., and Bazyn, T., 2012, "Engine Combustion Network (ECN): Measurements of Nozzle Geometry and Hydraulic Behavior," Atom. Sprays, **22**(12), pp. 1011–1052.

[26] Kastengren, A., and Powell, C. F., 2014, "Synchrotron X-ray Techniques for Fluid Dynamics," Exp. Fluids, **55**(3), p. 1686.

[27] Kastengren, A. L., Tilocco, F. Z., Duke, D., Powell, C. F., Zhang, X., and Moon, S., 2014, "Time-resolved X-ray Radiography of Sprays From Engine Combustion Network Spray a Diesel Injectors," Atom. Sprays, **24**(3), pp. 251–272.

[28] Ilavsky, J., Jemian, P. R., Allen, A. J., Zhang, F., Levine, L. E., and Long, G. G., 2009, "Ultra-small-angle X-ray Scattering At the Advanced Photon Source," J. Appl. Crystallogr., **42**(3), pp. 469–479.

[29] Matusik, K. E., Sforzo, B., Seong, H., Duke, D., Kastengren, A. L., Ilavsky, J., and Powell, C. F., 2019, "X-ray Measurements of Fuel Spray Specific Surface Area and Sauter Mean Diameter for Cavitating and Non-cavitating Diesel Sprays," Atom. Sprays, **29**(3), pp. 199–216.

[30] Als-Nielsen, J., and McMorrow, D., 2011, *Elements of Modern X-ray Physics*, John Wiley & Sons.

[31] Payri, R., Salvador, F. J., Marti-Aldaravi, P., and Vaquerizo, D., 2017, "Ecn Spray G External Spray Visualization and Spray Collapse Description Through Penetration and Morphology Analysis," Appl. Therm. Eng., **112**, pp. 304–316.

[32] Sphicas, P., Pickett, L. M., Skeen, S. A., and Frank, J. H., 2018, "Inter-plume Aerodynamics for Gasoline Spray Collapse," Int. J. Engine Res., **19**(10), pp. 1048–1067.

[33] Duke, D. J., Kastengren, A. L., Matusik, K. E., Swantek, A. B., Powell, C. F., Payri, R., Vaquerizo, D., Itani, L., Bruneaux, G., Grover, R. O., Parrish, S., Markle, L., Schmidt, D., Manin, J., Skeen, S. A., and Pickett, L. M., 2017, "Internal and Near Nozzle Measurements of Engine Combustion Network "spray G" Gasoline Direct Injectors," Exp. Therm Fluid Sci., **88**, pp. 608–621.

[34] Kastengren, A. L., Powell, C. F., Wang, Y., Im, K. -S., and Wang, J., 2009, "X-Ray Radiography Measurements of Diesel Spray Structure At Engine-Like Ambient Density," Atom. Sprays, **19**(11), pp. 1031–1044.

[35] Wang, Z., Swantek, A., Scarcelli, R., Duke, D., Kastengren, A., Powell, C. F., Som, S., Reese, R., Freeman, K., and Zhu, Y., 2015, "Les of Diesel and Gasoline Sprays With Validation Against X-ray Radiography Data," SAE Int. J. Fuels Lubr., **8**(1), pp. 147–159.

[36] Sforzo, B., Tekawade, A., Matusik, K., Kastengren, A., Ilavsky, J., Fezzaa, K., and Powell, C., 2019, "X-ray Characterization and Spray Measurements of ECN Spray G Using Alternative Fuels Under Flashing Conditions," ILASS Americas 30th Annual Conference on Liquid Atomization and Spray Systems, no. 61, ILASS Americas.

[37] Powell, C., Duke, D., Kastengren, A., and Ilavsky, J., 2013, "Measurements of Diesel Spray Droplet Size With Ultra-small Angle X-Ray Scattering," 25th ILASS-Americas conference, ILASS Americas.

[38] Kastengren, A., Ilavsky, J., Viera, J. P., Payri, R., Duke, D., Swantek, A., Tilocco, F. Z., Sovis, N., and Powell, C., 2017, "Measurements of Droplet Size in Shear-Driven Atomization Using Ultra-Small Angle X-Ray Scattering," Int. J. Multiphase Flow, **92**, pp. 131–139.

[39] Aleiferis, P., Serras-Pereira, J., van Romunde, Z., Caine, J., and Wirth, M., 2010, "Mechanisms of Spray Formation and Combustion From a Multi-Hole Injector With E85 and Gasoline," Combust. Flame, **157**(4), pp. 735–756.

[40] Aleiferis, P., and van Romunde, Z., 2013, "An Analysis of Spray Development With Iso-Octane, n-Pentane, Gasoline, Ethanol and n-Butanol From a Multi-Hole Injector Under Hot Fuel Conditions," Fuel, **105**, pp. 143–168.

[41] Parrish, S., 2014, "Gasoline Spray (Spray G) Topic 3.4, Drop Size Measurement," ECN3 Workshop, Engine Combustion Network.

[42] Li, Y., Guo, H., Ma, X., Wang, J., and Xu, H., 2016, "Droplet Dynamics of Di Spray From Sub-Atmospheric to Elevated Ambient Pressure," Fuel, **179**, pp. 25–35.